

Cite this: *J. Mater. Chem. A*, 2017, 5, 10827Received 14th January 2017  
Accepted 29th April 2017

DOI: 10.1039/c7ta00463j

rsc.li/materials-a

# Pseudocapacitive titanium oxynitride mesoporous nanowires with iso-oriented nanocrystals for ultrahigh-rate sodium ion hybrid capacitors†

Jun Dong,<sup>a</sup> Yalong Jiang,<sup>a</sup> Qidong Li,<sup>a</sup> Qiulong Wei,<sup>ID</sup>\*<sup>ab</sup> Wei Yang,<sup>a</sup> Shuangshuang Tan,<sup>a</sup> Xu Xu,<sup>a</sup> Qinyou An<sup>ID</sup><sup>a</sup> and Liqiang Mai<sup>ID</sup>\*<sup>ac</sup>

Titanium oxynitride mesoporous nanowires (Ti(O,N)-MP-NWs) composed of iso-oriented interconnected nanocrystals with [100] preferred orientation and tunable O/N ratios are synthesized, based on an anion exchange process. By investigating the electrochemical performance, it is found to exhibit high pseudocapacitive sodium storage performance, demonstrated by kinetic analysis and experimental characterizations. Subsequently, the assembled asymmetric hybrid sodium ion capacitor (AC//Ti(O,N)) exhibits high energy and power densities. Our work proposes the high pseudocapacitance in non-aqueous sodium ion system is very promising for high-power and low-cost energy storage applications.

## Introduction

The demand for green electrochemical energy storage (EES) devices is increasing for portable electronics, electric vehicles (EVs) and smart grids.<sup>1</sup> In particular, rechargeable lithium ion batteries (LIBs) and supercapacitors (SCs) have become the leading EES devices. Batteries usually show high energy density, while SCs deliver high power density.<sup>2–4</sup> However, future EES devices will require both high energy and power densities for applications in EVs and large-scale energy storage systems (the smart grids).<sup>5</sup> Therefore, the hybrid electrochemical capacitor (HEC), a new type of EES device that integrates the advantages of both batteries and SCs, is pointed out.<sup>6</sup> The HEC utilizes both faradaic and non-faradaic processes to store charge, for achieving improvements in both energy and power densities,

respectively. It usually combines a high specific surface area active carbon (AC) cathode (rapid charging rate) and a battery-like anode (large specific capacity). Lithium ion HECs (Li-HECs) have attracted intensive research interest.<sup>6</sup> However, owing to the rapidly increased prices and limited sources of lithium, the development of alternative sodium ion energy storage systems (such as sodium ion HECs, Na-HECs) with lower cost and comparable performance to lithium ion systems is urgently desired.<sup>7</sup>

To develop Na-HECs, the main challenge is the kinetics mismatch issue, which is usually much worse than that for Li-HECs. It is known that the radius of Na<sup>+</sup> is larger than that of Li<sup>+</sup> (0.97 vs. 0.68 Å),<sup>1,8</sup> meaning that various anode materials may not be suitable or exhibit lower specific capacity for sodium ion storage. More importantly, the Na<sup>+</sup> ion diffusion is much slower, which will enlarge the kinetics mismatch gap between the faradaic reaction controlled by ion diffusion and the fast non-faradaic double-layer adsorption/desorption of solvated ions in HEC devices.<sup>9</sup> Thus, to realize a high-rate anode, an alternative solution is to utilize a pseudocapacitive mechanism, whose kinetics are not diffusion-limited but are fast.<sup>10,11</sup> Transition metal oxides have shown high pseudocapacitance.<sup>2,12</sup> However, most transition metal oxides usually present poor electronic conductivity, which goes against the high rate capability.

Transition metal nitrides usually show superior electrical conductivity and sustainability, and are regarded as a potential candidate for energy storage applications.<sup>13–15</sup> Among them, TiN has received particular attention owing to its high conductivity (4000–55 000 S cm<sup>-1</sup>), as well as chemical and thermal stability.<sup>16–22</sup> TiN has shown good electrochemical performance in aqueous electrolytes,<sup>22–25</sup> but its energy density ( $E = 1/2CV^2$ ) is limited by the low output potential in aqueous electrolytes.<sup>11,17,26</sup> Replacing the aqueous electrolyte with a commercial non-aqueous electrolyte has the benefit of increasing the output voltage for the whole device. However, titanium nitrides are seldom investigated on this point, especially in sodium ion systems. Interestingly, a universal synthesis method for TiN is based on an anion exchange process that replaces the oxygen

<sup>a</sup>State Key Laboratory of Advanced Technology for Materials, Synthesis and Processing, International School of Materials Science and Engineering, Wuhan University of Technology, Wuhan 430070, China. E-mail: mlq518@whut.edu.cn; wql236@whut.edu.cn

<sup>b</sup>Department of Materials Science and Engineering, University of California Los Angeles, Los Angeles, CA 90095-1595, USA

<sup>c</sup>Department of Chemistry, University of California, Berkeley, California 94720, USA

† Electronic supplementary information (ESI) available: X-ray diffraction, cyclic voltammetry, morphology characterization, coulombic efficiency, energy dispersive X-ray spectroscopy. See DOI: 10.1039/c7ta00463j

atom in hydrogen titanate (or titanium oxide) precursors with a nitrogen atom under heat treatment in an ammonia atmosphere. The final products are usually oxygen-containing to some degree, so they are called titanium oxynitride (Ti(O,N)) as well.<sup>27–29</sup> Moreover, oxides will usually form on the Ti(O,N) surface in air or oxygen atmosphere, which are regarded as electrochemically active compounds. However, their detailed influence on electrochemical performance is rarely studied.

Herein, we present Ti(O,N) mesoporous nanowires (Ti(O,N)-MP-NWs) composed of iso-oriented nanocrystals as an anode for Na-HECs in non-aqueous electrolyte for the first time. The novel mesoporous nanowires offer a large surface area, short diffusion pathway and continual electron transport, which are beneficial for the charge storage process.<sup>30,33</sup> The Ti(O,N)-MP-NWs are synthesized based on an anion exchange process, while the oxygen content is tunable. We find that the oxygen in Ti(O,N) has a large influence on the electrochemical performance. Moreover, through kinetic analysis and *ex situ* characterization, the pseudocapacitive charge storage mechanism of Ti(O,N)-MP-NWs is demonstrated. Based on the designed materials, the asymmetric AC//Ti(O,N)-MP-NWs Na-HEC shows remarkably enhanced high power and energy densities, indicating the promise for fast sodium ion storage applications.

## Results and discussion

### Phase transformation and mesoporous formation

Fig. 1 schematically illustrates the phase transformation and mesoporous formation processes of the as-synthesized Ti(O,N)-

MP-NWs. Hydrogen titanate ( $\text{H}_2\text{Ti}_3\text{O}_7$ ) NWs of  $\sim 100$  nm in diameter and several micrometers in length were used as the precursor (Fig. 1b and S1, ESI<sup>†</sup>). The white precursor was annealed in ammonia flow (rate 80 sccm) with a heating rate of  $5^\circ\text{C min}^{-1}$ . By tuning the annealing time under ammonia flow at  $700^\circ\text{C}$ , the representative products were characterized by X-ray diffraction (XRD) (Fig. S2, ESI<sup>†</sup>), which demonstrates that the reactions consist of dehydration, phase transformation, and anion exchange processes.<sup>32–35</sup> In the first stage, the  $\text{H}_2\text{Ti}_3\text{O}_7$  NWs suffer a dehydration process accompanied by a phase transformation from white  $\text{H}_2\text{Ti}_3\text{O}_7$  (Fig. 1c) to olive  $\text{TiO}_2(\text{B})$  (Fig. 1e), with structural condensation. Meanwhile, mesoporous are formed in the NWs along with the dehydration and phase transformation process (Fig. 1d). In the second stage, the anion exchange process takes place, by substituting oxygen with nitrogen atoms, resulting in the formation of cubic Ti(O,N) phase, whose crystal form is similar to that of the TiN or TiO phase (Fig. 1g and S3, ESI<sup>†</sup>). Rich pores are formed in this process owing to the huge phase transformation and loss of oxygen atoms (Fig. 1f).

By tuning the annealing temperature, it is found that the anion exchange process is thermodynamically controlled (Fig. 2a). The sample annealed at  $600^\circ\text{C}$  for 2 hours results in  $\text{TiO}_2(\text{B})$  phase (JCPDS 74-1940), noted as  $\text{TiO}_2(\text{B})$ -600. However, the samples annealed at  $700^\circ\text{C}$  or  $800^\circ\text{C}$  for 2 hours are successfully converted to Ti(O,N), denoted as Ti(O,N)-700 and Ti(O,N)-800, respectively. The lattice parameters of cubic Ti(O,N)-700 and Ti(O,N)-800 are  $a_1 = 4.1780 \text{ \AA}$  and  $a_2 = 4.2012 \text{ \AA}$ , respectively. These parameters are both smaller than the

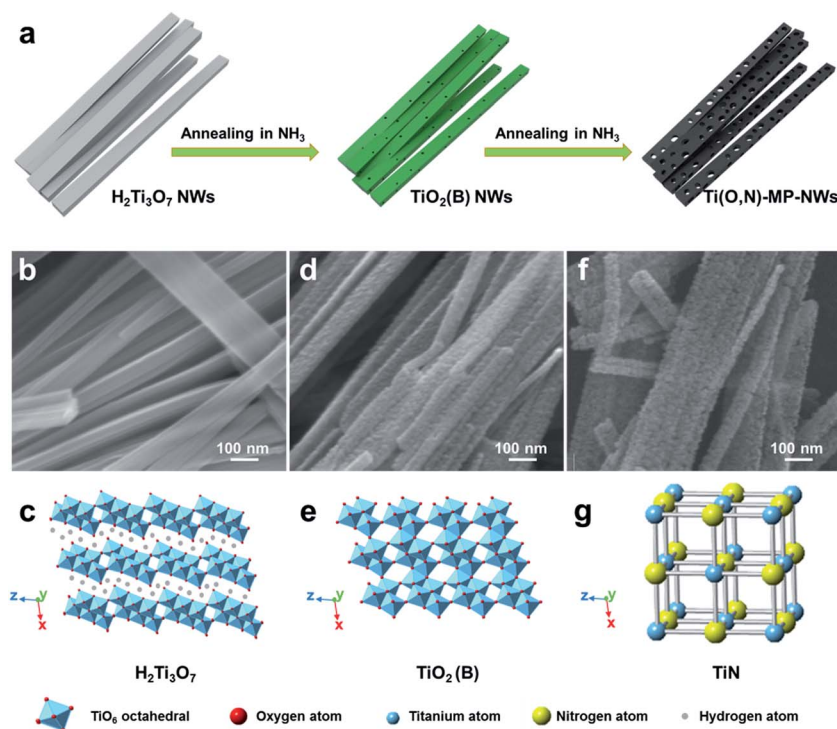


Fig. 1 (a) Schematic of proposed formation process for the titanium oxynitride mesoporous nanowires (Ti(O,N)-MP-NWs). SEM image (b) and crystal structure (c) of  $\text{H}_2\text{Ti}_3\text{O}_7$  nanowires. SEM image (d) and crystal structure (e) of  $\text{TiO}_2(\text{B})$ -MP-NWs. SEM image (f) of Ti(O,N)-MP-NWs and crystal structure (g) of TiN.

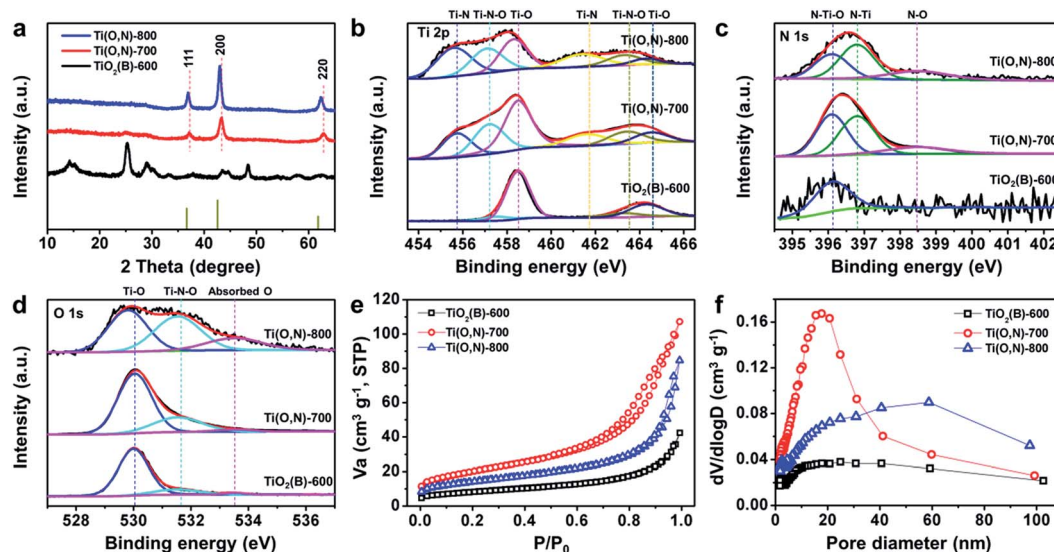


Fig. 2 XRD patterns (a) and XPS spectra of Ti 2p (b), N 1s (c) and O 1s (d). Nitrogen adsorption–desorption isotherms (e) and pore size distribution curves (f) of  $\text{TiO}_2(\text{B})$ -600,  $\text{Ti}(\text{O},\text{N})$ -700 and  $\text{Ti}(\text{O},\text{N})$ -800.

corresponding value of the standard cubic TiN ( $a = 4.2417 \text{ \AA}$ , JCPDS 38-1420) while larger than that of cubic TiO ( $a = 4.1770 \text{ \AA}$ , JCPDS 08-0117), thus consistent with the structural features of  $\text{Ti}(\text{O},\text{N})$ .<sup>35</sup> Interestingly, with increasing calcination temperature, the diffraction peaks shift towards lower angles (Fig. 2a), which is connected with the anion exchange degree. At lower annealing temperature (700 °C), the anion exchange kinetics are slower, which may create more oxygen residues, ion vacancies and structural defects.<sup>28,35</sup> The changes in the surface chemical composition were monitored by X-ray photoelectron spectroscopy (XPS) analysis (Fig. 2b–d). The Ti 2p spectra (Fig. 2b) included multiple peaks assigned to Ti–N ( $2p_{3/2} = 455.6$ – $455.7 \text{ eV}$  and  $2p_{1/2} = 461.4$ – $461.6 \text{ eV}$ ), Ti–N–O ( $2p_{3/2} = 457.1$ – $457.5 \text{ eV}$  and  $2p_{1/2} = 463.2$ – $463.4 \text{ eV}$ ), and Ti–O ( $2p_{3/2} = 458.3$ – $458.5 \text{ eV}$  and  $2p_{1/2} = 464.3$ – $464.5 \text{ eV}$ ).<sup>36,37</sup> The relative intensity of the Ti–O peak of  $\text{Ti}(\text{O},\text{N})$ -700 is significantly stronger than that of  $\text{Ti}(\text{O},\text{N})$ -800, indicating the higher valance state of Ti in  $\text{Ti}(\text{O},\text{N})$ -700. The N 1s spectra (Fig. 2c) of  $\text{Ti}(\text{N},\text{O})$  are deconvoluted into three synthetic peaks. The relative intensity of the N–Ti (396.1 eV) peak to the N–Ti–O peak (396.8 eV) is enlarged with increasing annealing temperature,<sup>35,38</sup> indicating increased nitridation degree at higher temperatures, consistent with the peak shift results in the XRD pattern. The O 1s spectra (Fig. 2d) are able to be fitted by three components as well. The peak of Ti–O ( $530 \pm 0.2 \text{ eV}$ ) is associated with oxidized titanium valence ( $\text{Ti}^{4+}$ ).<sup>37,39</sup> The relative ratio of Ti–O to Ti–N–O ( $531.5 \pm 0.2 \text{ eV}$ ) decreases with the increase of annealing temperature, which is consistent with the results of the Ti 2p spectra. As discussed above, the anion exchange kinetics depend on the annealing temperature. The slower ion exchange process at lower temperature leads to less exchange of O atoms being completed, leading to higher oxygen content and higher valence of Ti in  $\text{Ti}(\text{O},\text{N})$ -700.

Nitrogen adsorption–desorption isotherms and pore-size distributions were obtained to investigate the Brunauer–

Emmett–Teller (BET) specific surface areas (SSA) and porous structures of the samples. Fig. 2e exhibits typical type-IV curves, which are characteristic of mesoporous materials. The Barrett–Joyner–Halenda (BJH) pore size distribution curves (Fig. 2f) show that the pore sizes are mainly below 20 nm. A summary of the SSA, porous volume and BJH average porous size is listed in Table S1 (ESI<sup>†</sup>).  $\text{Ti}(\text{O},\text{N})$ -700 possesses larger SSA ( $70.75 \text{ m}^2 \text{ g}^{-1}$ ) than  $\text{TiO}_2(\text{B})$ -600 ( $29.02 \text{ m}^2 \text{ g}^{-1}$ ) because more vacancies are created during the anion exchange and phase transformation processes. The decrease of SSA for  $\text{Ti}(\text{O},\text{N})$ -800 ( $49.25 \text{ m}^2 \text{ g}^{-1}$ ), corresponding to the increase of the pore size, is possible owing to the increased mass transfer and accelerated crystal growth at high temperature.<sup>2,39</sup> The results are consistent with the morphology in Fig. 3a, S4 and S5 (ESI<sup>†</sup>).

Transmission electron microscopy (TEM) was carried out to identify the inner architecture and crystallographic structure of the samples. The TEM image of  $\text{Ti}(\text{O},\text{N})$ -700 (Fig. 3a) clearly shows typical mesoporous nanowires morphology, which is constituted of interconnected nanocrystalline grains. The high-resolution TEM (HRTEM) image of  $\text{Ti}(\text{O},\text{N})$ -700 (Fig. 3b) displays a  $d_{(200)}$  spacing of around 2.17 Å, which is slightly smaller than that of  $\text{Ti}(\text{O},\text{N})$ -800 ( $d_{(200)} \approx 2.19 \text{ \AA}$ , Fig. S5, ESI<sup>†</sup>), consistent with the XRD results (Fig. 2a). Interestingly, we find that the MP-NW consists of iso-oriented nanocrystalline grains with a continuous lattice fringe around the pores (Fig. 3b). The selected area electron diffraction (SAED) pattern (Fig. 3c) further confirms the single-crystal nature of the mesoporous NW. The SAED patterns (Fig. 3c and S5d<sup>†</sup>) reveals that the  $\text{Ti}(\text{O},\text{N})$ -MP-NW has a [100] preferred orientation along the axial direction of NW. As suggested by Bi *et al.*<sup>40</sup> the [100] direction has higher electronic transport than other directions. The as-synthesized  $\text{Ti}(\text{O},\text{N})$ -MP-NWs have optimized electrical conductivity that is beneficial for fast charge/discharge rates. Meanwhile, unlike other mesoporous materials with polycrystalline pore walls, the mesoporous NWs with iso-oriented interconnected

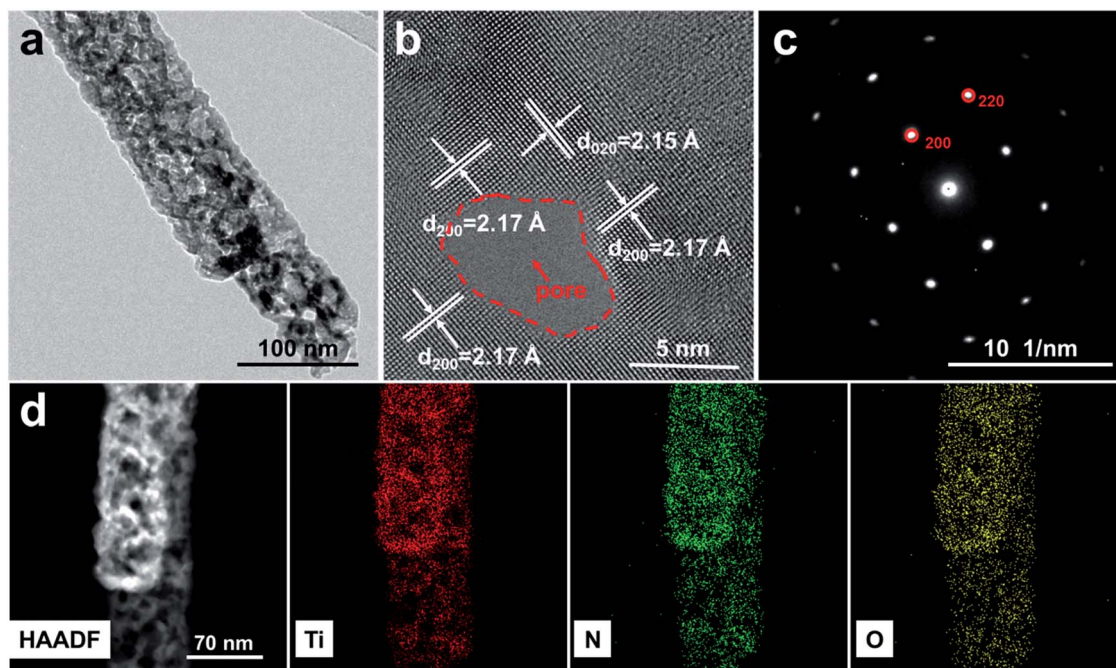


Fig. 3 Morphology characterization of Ti(O,N)-700. TEM image (a), HRTEM image (b), SAED pattern (c) and elemental mapping images (d).

nanocrystalline grains are able to reduce interfacial resistance and accelerate the rate of electron and ion transport.<sup>41–43</sup> The excellent conductivity is directly presented by measuring a single nanowire's conductivity. The inset of Fig. S6† shows the example of a Ti(O,N)-700 nanowire together with two deposited Au measuring contacts. Based on the *I*-*V* curve (Fig. S6, ESI†), the calculated average value is  $3 \times 10^6 \text{ S m}^{-1}$ , demonstrating the high conductivity of the Ti(O,N) nanowires. Elemental mappings (Fig. 3d) show a uniform distribution of Ti, N and O. Further, energy dispersive X-ray spectroscopy (EDS) data shows that the O/N ratio decreases from 1.27 to 0.51 when the temperature increases from 700 to 800 °C (Table S2, ESI†), confirming the higher oxygen content in Ti(O,N)-700.

### Electrochemical sodium ion storage performance

To explore the electrochemical performances, three samples were assembled into half-cells (2016-type coin cell) by using metallic sodium as the counter electrode. Noteworthy, the highly conductive Ti(O,N) were prepared without any other conductive additives, which is suitable for increasing the total energy density and investigation of the reaction mechanism. The electrochemical performances of the Ti(O,N)-MP-NWs were firstly characterized by cyclic voltammetry (CV) in the range 0.02–3.0 V *versus* Na<sup>+</sup>/Na at 0.2 mV s<sup>-1</sup> (Fig. 4a, S7 and S8, ESI†). The CV curves display a typical pseudocapacitor-like rectangle shape after the initial cycle. The high current response at low voltage and the irreversible capacity loss in the first cycle are possibly ascribed to the formation of a solid electrolyte interphase (SEI) layer.<sup>44,45</sup> The subsequent two cycles of Ti(O,N)-700 are well overlapped, indicating excellent reversibility. The galvanostatic charge–discharge curves of Ti(O,N)-700 at 0.05 A g<sup>-1</sup> (Fig. 4b) display a pseudo-linear voltage response in the work potential region.

For the practical application of EES devices, high rate capability and excellent cycling ability are both indispensable. Comparing the three samples (Fig. 4c), Ti(O,N)-700 shows the best rate performance. At 0.05 A g<sup>-1</sup>, Ti(O,N)-700 exhibits a specific capacity of 387 C g<sup>-1</sup>. Even at 8.0 A g<sup>-1</sup>, the specific capacity of Ti(O,N)-700 still remains at 127 C g<sup>-1</sup>, which is higher than that of Ti(O,N)-800 (92 C g<sup>-1</sup>) and TiO<sub>2</sub>(B)-600 (58 C g<sup>-1</sup>). Long-life cycling performance and high coulombic efficiency at 1.0 A g<sup>-1</sup> are subsequently shown in Fig. 4d and S9 (ESI†). All three samples exhibit excellent cycling performance, while Ti(O,N)-700 exhibits a higher capacity of 158 C g<sup>-1</sup> than those of Ti(O,N)-800 (120 C g<sup>-1</sup>) and TiO<sub>2</sub>(B)-600 (65 C g<sup>-1</sup>) after 5000 cycles. Note that the capacity retention of Ti(O,N)-700 with respect to the third discharge capacity is 73% after 5000 cycles.

### Sodium ion storage mechanism

The sodium ion storage mechanism was studied in depth to analyze the reason for the enhanced electrochemical performance of Ti(O,N)-700. Subsequently, electrochemical impedance (EIS) spectra were measured (Fig. 4e). The Nyquist plots are composed of a depressed semicircle (characteristic of charge transfer resistance) in the medium-frequency region followed by a slanted line (characteristic of ion diffusion resistance) in the low-frequency region. The much decreased charge transfer resistance ( $R_{ct}$ ) of Ti(O,N) compared to TiO<sub>2</sub>(B) confirms the fact that transition metal nitrides have high conductivity. However, the  $R_{ct}$  value decreases with increasing O/N ratio, which may be due to the increased electron conductivity of Ti(O,N)-800 compared to that of Ti(O,N)-700. Moreover, in the low frequency region, the slopes of typical linear shape are much higher than 45°, revealing that the electrochemical reaction is not mainly controlled by the diffusion process.<sup>11,46</sup>

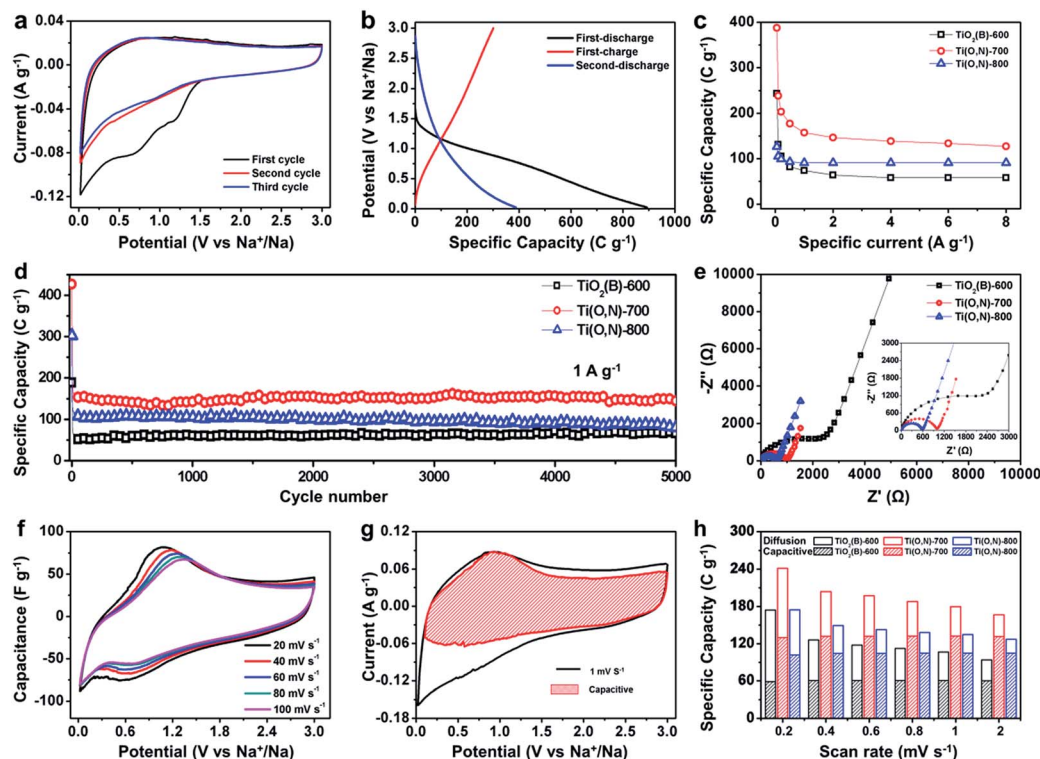


Fig. 4 (a) The CV curves of Ti(O,N)-700 at a scan rate of  $0.2 \text{ mV s}^{-1}$ . (b) Galvanostatic charge–discharge curves of Ti(O,N)-700 at  $0.05 \text{ A g}^{-1}$ . Rate performance (c), cycling performance at  $1 \text{ A g}^{-1}$  (d) and Nyquist plots (e) of  $\text{TiO}_2(\text{B})$ -600, Ti(O,N)-700 and Ti(O,N)-800. (f) CV curves of the Ti(O,N)-700 electrode at 20–100  $\text{mV s}^{-1}$ . (g) CV curves and related capacitive contribution curves of the Ti(O,N)-700 electrode at  $1 \text{ mV s}^{-1}$ . (h) Contributions of capacitive and diffusion-control capacities at different scan rates.

The CV curves of the Ti(O,N)-700 electrode at fast scan rates are shown in Fig. 4f. With increasing scan rate, even to  $100 \text{ mV s}^{-1}$ , the minor change of the curves reveals excellent rate performance. To quantify the capacitive contribution to the current response, the total current response ( $I$ ) at a fixed potential ( $V$ ) can be separated into two parts, according to eqn (1):<sup>11</sup>

$$I(V) = k_1\nu + k_2\nu^{1/2} \quad (1)$$

where  $k_1\nu$  and  $k_2\nu^{1/2}$  correspond to the capacitive and diffusion-controlled faradaic current responses, respectively. Fig. 4g shows the contribution of diffusion-limited and capacitive processes. The shaded area corresponds to the capacitive current response in comparison with the total current response at  $1 \text{ mV s}^{-1}$ . It is observed that the capacitive contributions occupy a large part of whole capacity. The redox peaks shown in the shaded area are related to the capacitive behaviors. At fast scan rates, the redox peaks are more obvious (Fig. S10, ESI†), owing to faster kinetics of the capacitive response compared to the diffusion one. The intuitionistic comparisons about the total stored charge and capacitive contributions at different scan rate are shown in Fig. 4h and S11 (ESI†). Ti(O,N)-700 shows a higher capacitive capacity ( $\approx 131 \text{ C g}^{-1}$ ) than those of  $\text{TiO}_2(\text{B})$ -600 ( $\approx 60 \text{ C g}^{-1}$ ) and Ti(O,N)-800 ( $\approx 104 \text{ C g}^{-1}$ ). Again, both capacitive contributions of Ti(O,N)-700 and Ti(O,N)-800 are similar and very high, about 78.9% and 82.3% of the total stored

charge at  $2 \text{ mV s}^{-1}$ , respectively. Typically, capacitive capacity includes electric double-layer capacity and pseudocapacitive capacity. It is worth noting that electric double-layer capacitance highly depends on a high SSA (typically  $>1500 \text{ m}^2 \text{ g}^{-1}$ ), which is usually assumed to be a value of  $10 \mu\text{F cm}^{-2}$  (ref. 47–49). The SSA of Ti(O,N)-700 and Ti(O,N)-800 are 70.75 and  $49.25 \text{ m}^2 \text{ g}^{-1}$ , respectively, referring to the electric double-layer capacities of  $\sim 21$  and  $15 \text{ C g}^{-1}$ , respectively, which are less than 5% of their measured capacity at  $0.05 \text{ A g}^{-1}$ . Moreover, since the rate capacity of an electric double-layer capacitor is usually excellent and we assume that the rate values will remain high up to  $8.0 \text{ A g}^{-1}$ , but this value ( $\sim 21 \text{ C g}^{-1}$ ) is still much less than the obtained capacity of  $127 \text{ C g}^{-1}$  for Ti(O,N)-700. Therefore, the majority of the capacity for Ti(O,N) is able to be attributed to reversible faradaic pseudocapacitive processes. Furthermore, the difference in capacity between Ti(O,N)-700 and Ti(O,N)-800 is compared in detail. The increased capacity of Ti(O,N)-700 compared to Ti(O,N)-800 is much larger than the difference in the values of their electric double-layer capacity (only  $6 \text{ C g}^{-1}$  based on above calculation). Therefore, the large increased capacitance for Ti(O,N)-700 is not likely to be from the enlarged SSA but from the pseudocapacitive charge storage.<sup>50</sup>

In a complementary analysis, the sodium storage mechanism of Ti(O,N) was further confirmed by *ex situ* XRD and TEM. Fig. 5a shows the *ex situ* XRD patterns of Ti(O,N)-700 at various states in the first two cycles (the voltage profile is displayed on the right side). The diffraction peaks of Ti(O,N) obtained at

different charge–discharge states are almost the same as that of the fresh Ti(O,N)-700 electrode without apparent peak change or shift, which means no obvious phase transformation takes place in the inner structure during charge and discharge process. Fig. 5b shows the Nyquist plots at different cycles for Ti(O,N)-700. The diameter of the depressed semicircle after activation obviously decreases, which means that lower  $R_{ct}$  is maintained during the following electrochemical reaction. It also suggests a stable electrode–electrolyte interface during cycles without increased SEI film generation.<sup>30</sup> At the same time, the reduction of the  $R_{ct}$  is conducive to the stability during subsequent cycles and capacity retention at high rate.<sup>30,31</sup>

The morphology and structure of Ti(O,N)-700 in the fully discharged state were further characterized by TEM (Fig. 5c). The nanowire morphology remained pretty well after discharge. The clear lattice fringe with  $d_{(200)}$  value of 2.18 Å (Fig. 5d) is clearly observed, indicating that there are no obvious phase transformations in the inner structure, consistent with the *ex situ* XRD results. The slightly enlarged  $d_{(200)}$  value compared to the fresh one (Fig. 3b) is probably owing to the fact that reduced state of the titanium cation (caused by the faradaic redox reaction) has a larger ionic radius than that of the oxidized state. Element mappings (Fig. 5e) display the uniform distribution of Ti, N and O after sodiation. These results match well with kinetic analysis as discussed before and demonstrate that the charge storage of Ti(N,O) is *via* a pseudocapacitive mechanism without phase changes.

Based on the above analysis, the Ti(O,N)-700 with high O/N ratio and high Ti valence state provides more charge transfer numbers during the faradaic reaction, and therefore exhibits enhanced electrochemical performance.

### Sodium ion hybrid electrochemical capacitor

This rapid pseudocapacitance leads to the remarkable rate performance of Ti(O,N), making it very promising as an anode for Na-HEC. A schematic of the asymmetrical Na-HEC is shown in Fig. 6a. The hybrid supercapacitor uses a non-faradaic capacitive cathode (AC) whose charge storage is based on electrical double layer adsorption/desorption of  $\text{ClO}_4^-$  anion, and a faradaic redox anode (Ti(O,N)) that is based on a reversible pseudocapacitive process with  $\text{Na}^+$  cation. According to the capacity balance between the Ti(O,N) anode and the AC cathode (Fig. S12, ESI†), the mass ratio of 1 : 1.5 (anode : cathode) is fixed. The CV curve of the Na-HEC in the range from 0.5 to 4 V at  $0.2 \text{ mV s}^{-1}$  (Fig. S13, ESI†) exhibits a rectangular shape, indicating that the majority of the capacity is ascribed to capacitive behavior.<sup>11,17</sup> The Nyquist plots and Bode diagram with frequencies ranging from 0.01 Hz to 100 kHz are shown in Fig. S14 (ESI†). An almost vertical line at low frequencies and  $|\phi_{0.01\text{Hz}}| = 70.3^\circ$  are observed, which demonstrates typical capacitive behavior.<sup>51</sup> Moreover, the frequency at  $\phi = -45^\circ$ , corresponding to the capacitor response frequency, is 0.47 Hz. The corresponding time constant is 2.1 s, which is much shorter than 10 s for the traditional active carbon supercapacitors.<sup>52</sup> Fig. 6b shows the charge and discharge curves for Na-HEC over the range 0.5–4 V at  $1 \text{ A g}^{-1}$  (based on the mass of Ti(O,N)). After activation at  $0.05 \text{ A g}^{-1}$  for two cycles, the Na-HEC device delivers a reversible capacity of  $140 \text{ C g}_{\text{Ti(O,N)}}^{-1}$  based on the mass of Ti(O,N) (corresponding to  $56 \text{ C g}_{\text{FC}}^{-1}$  based on the total mass of both active materials). The Na-HEC exhibits an average operating voltage of  $\sim 2.6 \text{ V}$ , much higher than that of other aqueous HECs ( $\sim 1.23 \text{ V}$ ).<sup>53</sup>

The cycling stability and rate performance of the device were characterized (Fig. 6c and d). The capacity retention was 82.9%

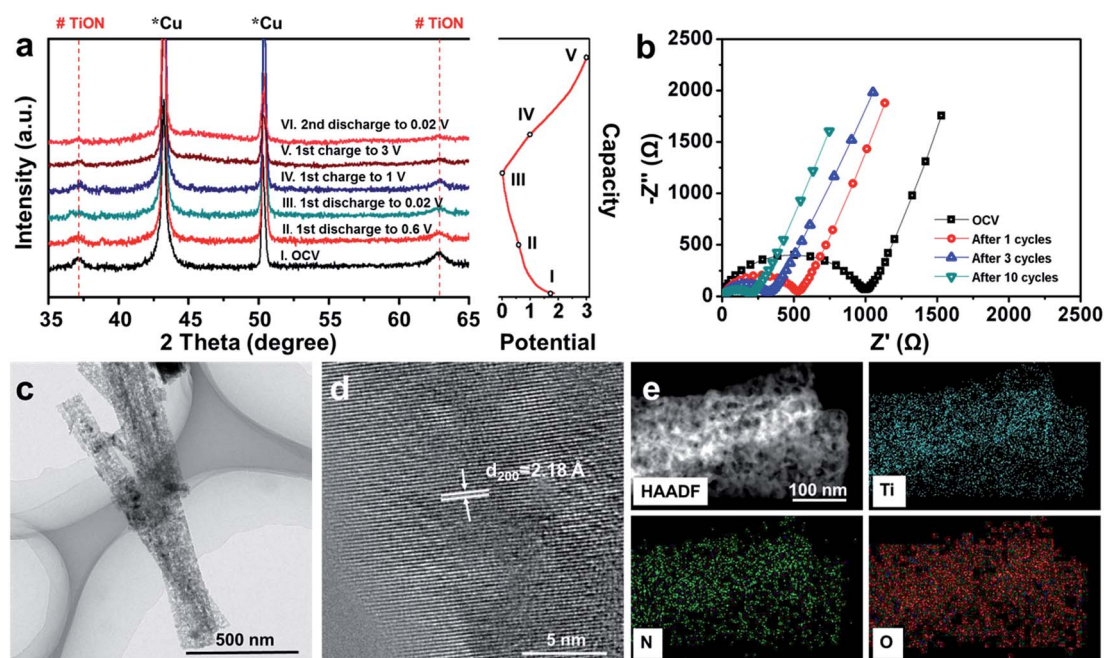


Fig. 5 (a) *Ex situ* XRD of Ti(O,N)-700 in different charge–discharge states. (b) Nyquist plots of Ti(O,N)-700 in different cycles. (c–e) Morphology characterization of Ti(O,N)-700 electrode at a fully discharged state: TEM image (c), HRTEM image (d), and elemental mapping images (e).

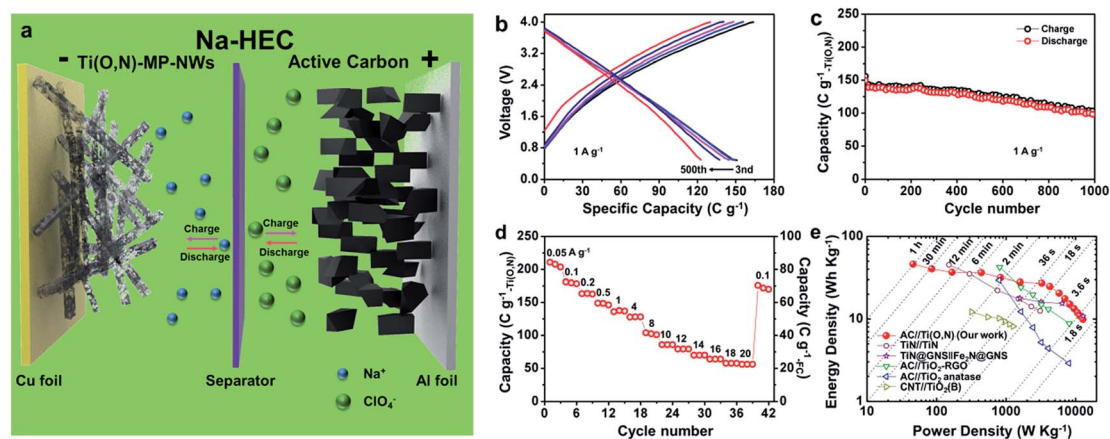


Fig. 6 Electrochemical performance of Ti(O,N)//AC hybrid full capacitor. (a) Schematic of the AC//Ti(O,N)-MP-NWs Na-HEC. Charge/discharge curves (b), cycling performance (c), and rate performance (d) of Na-HEC. (e) Ragone plots of various supercapacitors. The Na-HEC based on AC//Ti(O,N)-MP-NWs is compared with other supercapacitors using TiN//TiN,<sup>56</sup> TiN@GNS//Fe<sub>2</sub>N@GNS,<sup>17</sup> AC//TiO<sub>2</sub>-RGO,<sup>9</sup> AC//TiO<sub>2</sub> (anatase)<sup>9</sup> and CNT//TiO<sub>2</sub>(B).<sup>57</sup>

after 500 cycles, and a capacity of  $98 \text{ C g}_{\text{Ti(O,N)}}^{-1}$  was retained after 1000 cycles with high coulombic efficiency (Fig. S15, ESI<sup>†</sup>), indicating very good reversibility during the charge–discharge process. The rate capacity of the device is subsequently shown in Fig. 6d. The discharge-specific capacities of the Na-HEC are about  $205 \text{ C g}_{\text{Ti(O,N)}}^{-1}$  ( $82 \text{ C g}_{\text{FC}}^{-1}$ ) at  $0.05 \text{ A g}^{-1}$  and  $100 \text{ C g}_{\text{Ti(O,N)}}^{-1}$  ( $40 \text{ C g}_{\text{FC}}^{-1}$ ) at  $8 \text{ A g}^{-1}$ . Eventually, the capacity is still  $56 \text{ C g}_{\text{Ti(O,N)}}^{-1}$  ( $22 \text{ C g}_{\text{FC}}^{-1}$ ) at extremely high current density (up to  $20 \text{ A g}^{-1}$ ), indicating that the device is promising for achieving high rate capacity. The static leakage current of the Na-HEC is about  $4 \mu\text{A}$  ( $3.8 \mu\text{A mg}^{-1}$ ), indicating a relatively small leakage current (Fig. S16, ESI<sup>†</sup>).<sup>54,55</sup>

Energy density and power density based on the values from the charge–discharge curves at different current densities were calculated (according to the total mass of both active materials), as shown by the Ragone plots (Fig. 6e). For comparison, the energy and power densities of state-of-the-art TiN//TiN,<sup>56</sup> TiN@GNS//Fe<sub>2</sub>N@GNS,<sup>17</sup> AC//TiO<sub>2</sub>-RGO,<sup>9</sup> AC//TiO<sub>2</sub> (anatase),<sup>9</sup> and CNT//TiO<sub>2</sub>(B)<sup>57</sup> are plotted together in Fig. 6e. Ragone plots demonstrate AC//Ti(O,N)-MP-NWs Na-HEC delivers the highest energy density at high power density among similar systems. Detailed data for the various EES devices are shown in Table S3, ESI<sup>†</sup>. A maximum energy density of  $46 \text{ W h kg}^{-1}$  is achieved at a power density of  $46 \text{ W kg}^{-1}$ . When the power density increases to  $11.5 \text{ kW kg}^{-1}$ , the energy density is  $10.9 \text{ W h kg}^{-1}$ , with a drain time of only  $\sim 3.4 \text{ s}$ . The obtained data demonstrate that the as-assembled AC//Ti(O,N)-MP-NWs Na-HEC is a very promising energy storage device with high power and energy density.

## Conclusion

Ti(O,N)-MP-NWs are synthesized *via* dehydration, phase transformation, and anion exchange processes in ammonia flow. The Ti(O,N)-MP-NWs are composed of iso-oriented interconnected nanocrystalline grains with [100] preferred orientation along the axial direction and tunable O/N ratios. Benefiting from the highly

conductive nature of Ti(O,N) and the largely increased surface redox sites and short ion diffusion pathways, the Ti(O,N)-MP-NWs display remarkable electrochemical performance. According to kinetic analysis and a series of *ex situ* characterizations, the pseudocapacitive behavior of Ti(O,N)-MP-NWs in sodium-based non-aqueous electrolyte is demonstrated. The large capacitive contribution is highly beneficial to the high-rate sodium storage performance. The high O/N ratio with the high valence state of Ti provides more charge transfer numbers during the faradaic reaction process, resulting in higher capacity. Based on the rapid pseudocapacitive charge storage, the as-assembled AC//Ti(O,N)-MP-NWs Na-HEC shows a maximum energy density of  $46 \text{ W h kg}^{-1}$  (with a power density of  $46 \text{ W kg}^{-1}$ ) and power density of  $11.5 \text{ kW kg}^{-1}$  (with an energy density of  $10.9 \text{ W h kg}^{-1}$ ) indicating great promise for applications in high-rate energy storage fields. We believe the present work will open a new window for developing pseudocapacitive electrode materials for high-rate energy storage applications.

## Acknowledgements

This work was supported by the National Key Research and Development Program of China (2016YFA0202603), the National Natural Science Foundation of China (51521001, 51602239), the National Natural Science Fund for Distinguished Young Scholars (51425204), the Hubei Provincial Natural Science Foundation of China (2016CFB267), the Fundamental Research Funds for the Central Universities (WUT:2017III009, 2017III005, 2017III007, 2017III030), and the International Postdoctoral Exchange Fellowship Program (20160025). Prof. Liqiang Mai gratefully acknowledges financial support from the China Scholarship Council (No. 201606955096).

## Notes and references

- 1 D. Kundu, E. Talaie, V. Duffort and L. F. Nazar, *Angew. Chem., Int. Ed.*, 2015, **54**, 3431.

- 2 Y. Wang, Y. Song and Y. Xia, *Chem. Soc. Rev.*, 2016, **45**, 5925.
- 3 J. M. Tarascon and M. Armand, *Nature*, 2001, **414**, 359.
- 4 X. Xia, D. Chao, C. F. Ng, J. Lin, Z. Fan, H. Zhang, Z. X. Shen and H. J. Fan, *Mater. Horiz.*, 2015, **2**, 237.
- 5 K. Kang, Y. S. Meng, J. Breger, C. P. Grey and G. Ceder, *Science*, 2006, **311**, 977.
- 6 V. Aravindan, J. Gnanaraj, Y. S. Lee and S. Madhavi, *Chem. Rev.*, 2014, **114**, 11619.
- 7 N. Yabuuchi, M. Kajiyama, J. Iwatate, H. Nishikawa, S. Hitomi, R. Okuyama, R. Usui, Y. Yamada and S. Komaba, *Nat. Mater.*, 2012, **11**, 512.
- 8 H. Pan, Y.-S. Hu and L. Chen, *Energy Environ. Sci.*, 2013, **6**, 2338.
- 9 H. Kim, M.-Y. Cho, M.-H. Kim, K.-Y. Park, H. Gwon, Y. Lee, K. C. Roh and K. Kang, *Adv. Energy Mater.*, 2013, **3**, 1500.
- 10 V. Augustyn, J. Come, M. A. Lowe, J. W. Kim, P. L. Taberna, S. H. Tolbert, H. D. Abruna, P. Simon and B. Dunn, *Nat. Mater.*, 2013, **12**, 518.
- 11 V. Augustyn, P. Simon and B. Dunn, *Energy Environ. Sci.*, 2014, **7**, 1597.
- 12 H. Choi and H. Yoon, *Nanomaterials*, 2015, **5**, 906.
- 13 T. An, J. Tang, Y. Zhang, Y. Quan, X. Gong, A. M. Al-Enizi, A. A. Elzatahry, L. Zhang and G. Zheng, *ACS Appl. Mater. Interfaces*, 2016, **8**, 12772.
- 14 X. Xiao, X. Peng, H. Jin, T. Li, C. Zhang, B. Gao, B. Hu, K. Huo and J. Zhou, *Adv. Mater.*, 2013, **25**, 5091.
- 15 M.-S. Balogun, W. Qiu, W. Wang, P. Fang, X. Lu and Y. Tong, *J. Mater. Chem. A*, 2015, **3**, 1364.
- 16 B. Avsarala and P. Haldar, *Electrochim. Acta*, 2010, **55**, 9024.
- 17 C. Zhu, P. Yang, D. Chao, X. Wang, X. Zhang, S. Chen, B. K. Tay, H. Huang, H. Zhang, W. Mai and H. J. Fan, *Adv. Mater.*, 2015, **27**, 4566.
- 18 T. An, J. Tang, Y. Zhang, Y. Quan, X. Gong, A. M. Al-Enizi, A. A. Elzatahry, L. Zhang and G. Zheng, *ACS Appl. Mater. Interfaces*, 2016, **8**, 12772.
- 19 P. Sun, R. Lin, Z. Wang, M. Qiu, Z. Chai, B. Zhang, H. Meng, S. Tan, C. Zhao and W. Mai, *Nano Energy*, 2017, **31**, 432.
- 20 M.-S. Balogun, C. Li, Y. Zeng, M. Yu, Q. Wu, M. Wu, X. Lu and Y. Tong, *J. Power Sources*, 2014, **272**, 946.
- 21 M. S. Balogun, M. Yu, C. Li, T. Zhai, Y. Liu, X. Lu and Y. Tong, *J. Mater. Chem. A*, 2014, **2**, 10825.
- 22 Z. Chai, N. Zhang, P. Sun, Y. Huang, C. Zhao, H. J. Fan, X. Fan and W. Mai, *ACS Nano*, 2016, **10**, 9201.
- 23 D. Choi and P. N. Kumta, *J. Electrochem. Soc.*, 2006, **153**, A2298.
- 24 D. Sun, J. Lang, X. Yan, L. Hu and Q. Xue, *J. Solid State Chem.*, 2011, **184**, 1333.
- 25 P. Yang, D. Chao, C. Zhu, X. Xia, Y. Zhang, X. Wang, P. Sun, B. K. Tay, Z. X. Shen, W. Mai and H. J. Fan, *Adv. Sci.*, 2016, **3**, 1500299.
- 26 T. W. Lin, C. S. Dai and K. C. Hung, *Sci. Rep.*, 2014, **4**, 7274.
- 27 T. T. Chen, H. P. Liu, Y. J. Wei, I. C. Chang, M. H. Yang, Y. S. Lin, K. L. Chan, H. T. Chiu and C. Y. Lee, *Nanoscale*, 2014, **6**, 5106.
- 28 E. Martínez-Ferrero, Y. Sakatani, C. Boissière, D. Grosso, A. Fuertes, J. Fraxedas and C. Sanchez, *Adv. Funct. Mater.*, 2007, **17**, 3348.
- 29 L. Yan, G. Chen, S. Tan, M. Zhou, G. Zou, S. Deng, S. Smirnov and H. Luo, *ACS Appl. Mater. Interfaces*, 2015, **7**, 24212.
- 30 L. Mai, Q. Wei, Q. An, X. Tian, Y. Zhao, X. Xu, L. Xu, L. Chang and Q. Zhang, *Adv. Mater.*, 2013, **25**, 2969.
- 31 Q. Wei, Q. An, D. Chen, L. Mai, S. Chen, Y. Zhao, K. M. Hercule, L. Xu, A. Minhas-Khan and Q. Zhang, *Nano Lett.*, 2014, **14**, 1042.
- 32 K. Kamiya, T. Yoko and M. Bessho, *J. Mater. Sci.*, 1987, **22**, 937.
- 33 Y. Djaoued, R. Taj, R. Brüning, S. Badilescu, P. Ashrit, G. Bader and T. Vo-Van, *J. Non-Cryst. Solids*, 2002, **297**, 55.
- 34 E. Morgado Jr, P. M. Jardim, B. A. Marinkovic, F. C. Rizzo, M. A. de Abreu, J. L. Zotin and A. S. Araujo, *Nanotechnology*, 2007, **18**, 495710.
- 35 M. Sluban, P. Umek, Z. Jagličić, J. Buh, P. Šmitek, A. Mrzel, C. Bittencourt, P. Guttman, M. H. Delville, D. Mihailović and D. Arčon, *ACS Nano*, 2015, **9**, 10133.
- 36 X. Lu, G. Wang, T. Zhai, M. Yu, S. Xie, Y. Ling, C. Liang, Y. Tong and Y. Li, *Nano Lett.*, 2012, **12**, 5376.
- 37 M.-H. Chan and F.-H. Lu, *Thin Solid Films*, 2009, **517**, 5006.
- 38 N. C. Saha and H. G. Tompkins, *J. Appl. Phys.*, 1992, **72**, 3072.
- 39 M. Braic, M. Balaceanu, A. Vladescu, A. Kiss, V. Braic, G. Epurescu, G. Dinescu, A. Moldovan, R. Birjega and M. Dinescu, *Appl. Surf. Sci.*, 2007, **253**, 8210.
- 40 W. Bi, Z. Hu, X. Li, C. Wu, J. Wu, Y. Wu and Y. Xie, *Nano Res.*, 2014, **8**, 193.
- 41 T. Brezesinski, J. Wang, S. H. Tolbert and B. Dunn, *Nat. Mater.*, 2010, **9**, 146.
- 42 Y. Liu, R. Che, G. Chen, J. Fan, Z. Sun, Z. Wu, M. Wang, B. Li, J. Wei and Y. Wei, *Sci. Adv.*, 2015, **1**, e1500166.
- 43 T. Brezesinski, M. Groenewolt, N. Pinna, H. Amenitsch, M. Antonietti and B. Smarsly, *Adv. Mater.*, 2006, **18**, 1827.
- 44 M. D. Slater, D. Kim, E. Lee and C. S. Johnson, *Adv. Funct. Mater.*, 2013, **23**, 947.
- 45 A. Ponrouch, E. Marchante, M. Courty, J.-M. Tarascon and M. R. Palacin, *Energy Environ. Sci.*, 2012, **5**, 8572.
- 46 Q. Li, Q. Wei, Q. Wang, W. Luo, Q. An, Y. Xu, C. Niu, C. Tang and L. Mai, *J. Mater. Chem. A*, 2015, **3**, 18839.
- 47 A. K. Shukla, S. Sampath and K. Vijayamohan, *Curr. Sci.*, 2000, **79**, 1656.
- 48 A. G. Pandolfo and A. F. Hollenkamp, *J. Power Sources*, 2006, **157**, 11.
- 49 D. Sheberla, J. C. Bachman, J. S. Elias, C. J. Sun, Y. Shao-Horn and M. Dineen, *Nat. Mater.*, 2017, **16**, 220.
- 50 R. L. Porto, R. Frappier, J. B. Ducros, C. Aucher, H. Mosqueda, S. Chenu, B. Chavillon, F. Tessier, F. Cheviré and T. Brousse, *Electrochim. Acta*, 2012, **82**, 257.
- 51 R. Ding, L. Qi, M. Jia and H. Wang, *Electrochim. Acta*, 2013, **107**, 494.
- 52 M. F. El-Kady, V. Strong, S. Dubin and R. B. Kaner, *Science*, 2012, **335**, 1326–1330.
- 53 F. Beguin, V. Presser, A. Balducci and E. Frackowiak, *Adv. Mater.*, 2014, **26**, 2219.

- 54 H. Gao, L. Xiao, I. Plumel, G. L. Xu, Y. Ren, X. Zuo, Y. Liu, C. Schulz, H. Wiggers, K. Amine and Z. Chen, *Nano Lett.*, 2017, **17**, 1512.
- 55 C. Yang, L. Zhang, N. Hu, Z. Yang, H. Wei, Y. Wang and Y. Zhang, *Appl. Surf. Sci.*, 2016, **387**, 666.
- 56 S. Dong, X. Chen, L. Gu, X. Zhou, H. Xu, H. Wang, Z. Liu, P. Han, J. Yao, L. Wang, G. Cui and L. Chen, *ACS Appl. Mater. Interfaces*, 2011, **3**, 93.
- 57 Q. Wang, Z. H. Wen and J. H. Li, *Adv. Funct. Mater.*, 2006, **16**, 2141.